

A coculture based, 3D bioprinted ovarian tumor model combining cancer cells and cancer associated fibroblasts.

Zakaria Baka¹, Claire Godier¹, Laureline Lamy^{2,3}, Abhik Mallick¹, Varvara Gribova^{4,5}, Agathe Figarol⁶, Lina Bezdetnaya^{2,3}, Alicia Chateau², Zoé Magne¹, Marie Stiefel¹, Dounia Louaguef¹, Philippe Lavalle⁴, Eric Gaffet¹, Olivier Joubert¹, Halima Alem^{1,7}*

¹Institut Jean Lamour (IJL), Centre National de la Recherche Scientifique (CNRS), UMR 7198, Université de Lorraine, Campus Artem, 2 allée André Guinier, 54011 Nancy, France.

²Centre de Recherche en Automatique de Nancy (CRAN), Centre National de la Recherche Scientifique (CNRS), UMR 7039, Université de Lorraine, Campus Sciences, Boulevard des Aiguillettes, 54506 Vandoeuvre-lès-Nancy, France.

³Département Recherche, Institut de Cancérologie de Lorraine (ICL), 6 Avenue de Bourgogne, 54519 Vandoeuvre-lès-Nancy, France.

⁴Institut National de la Santé et de la Recherche Médicale (INSERM) U1121, Biomaterials and Bioengineering, 1 rue Eugène Boeckel, 67100 Strasbourg, France.

⁵Faculté de Chirurgie Dentaire, Université de Strasbourg, 8 rue Sainte Elisabeth, 67000 Strasbourg, France.

⁶Institut FEMTO ST, Centre National de la Recherche Scientifique (CNRS), UMR 6174, Université Bourgogne Franche Comté, 15B Avenue des Montboucons, F-25000 Besançon, France.

⁷Institut Universitaire de France

Corresponding author: Halima.alem@univ-lorraine.fr

Keywords: Ovarian cancer, 3D bioprinting, Preclinical model, Tumor microenvironment.

Abstract:

Ovarian cancer remains a major public health issue due to its poor prognosis. To develop more effective therapies, it is crucial to set-up reliable models that closely mimic the complexity of the ovarian tumor's microenvironment. 3D bioprinting is currently a promising approach to build heterogenous and reproducible cancer models with controlled shape and architecture.

However, this technology is still poorly investigated to model ovarian tumors. In this study, we describe a 3D bioprinted ovarian tumor model combining cancer cells (SKOV-3) and cancer associated fibroblasts (CAFs). The resulting tumor models showed their ability to maintain cell viability and proliferation. Cells were observed to self-assemble in heterotypic aggregates. Moreover, CAFs were observed to be recruited and to circle cancer cells reproducing an *in vivo* process taking place in the tumor microenvironment (TME). Interestingly, this approach also showed its ability to rapidly generate a high number of reproducible tumor models that could be subjected to usual characterizations (cell viability and metabolic activity; histology and immunological studies; and real-time imaging). Therefore, these ovarian tumor models can be an interesting tool for high throughput drug screening applications.

1. Introduction:

Ovarian cancer, being the 8th most frequent cancer in women[1], is a major public health issue. Its poor prognosis makes it the most lethal gynecological cancer [2,3]. This poor outcome is predominantly related to its frequent relapses and early abdominal dissemination[4]. Therefore, using adequate preclinical models of ovarian cancer is of major importance to elucidate its cellular and molecular mechanisms and further develop more effective therapies. Conventional monolayer cell culture is still widely used to study ovarian cancer[5], however, cells cultured in such 2D conditions do not faithfully reproduce the *in vivo* pathophysiological processes[6]. Indeed, tumors developing in the human body are three dimensional, highly complex structures where cancer cells closely interact with other elements of the tumoral microenvironment (TME)[7]. The TME notably includes cancer associated fibroblasts (CAFs), endothelial cells, immune cells and extracellular matrix (ECM) molecules[8]. These elements play crucial roles in cancer pathophysiology. For example, in ovarian cancer, CAFs were shown to be involved in cell invasion[9], metastasis[9] and drug resistance[10]. It is thus becoming urgent to develop more relevant preclinical models where the interactions between cancer cells and other TME elements are better emulated. 3D cell culture technologies have been widely investigated to bridge the gap between 2D cultures and the *in vivo* conditions[11]. These technologies notably include spheroids, organoids and 3D bioprinting. Spheroids usually consist of auto-assembled aggregates obtained in non-adherent surfaces or using gyratory rotation techniques[12]. While these structures can reproduce nutrient and oxygen gradients of human tumors, it is difficult to control their size and architecture[13]. Cancer organoids are generated using patient derived

cancer cells that are cultured in ECM-derived hydrogels such as Matrigel®[14]-[15]. The so obtained structures could reproduce phenotypic and genotypic features of the original tumors[16,17] and were used for personalized medicine applications[18]. However, as well as for spheroids, it can be challenging to create organoids with a controlled size and a predefined architecture. Moreover, the necessity of numerous growth factors makes organoid culture relatively expensive[19]. Nowadays, 3D bioprinting (also known as additive manufacturing) is emerging as a powerful tool to build complex 3D cancer models[20]. In this approach, a combination of cells and biocompatible materials (referred to as bioink) is used to create 3D constructs via a computer assisted layer-by-layer deposition process[21]. Due to this computer numerical control, it is possible to achieve structures with a complex, customizable and reproducible architecture. Moreover, it is possible to include several cell types within a single bioink. This allows a better mimicry of the TME cell diversity. In addition, 3D bioprinted structures can include perfusable network for long term culture processing[22]. During the last years, several 3D bioprinted models have been reported for human organs such as liver[23] and skin[24] as well as for major cancer types including lung cancers[25], breast cancers[26] and glioblastoma[27,28]. Through these studies, 3D bioprinting was shown as a powerful method to build relevant *in vivo*-like tumor constructs for different applications. However, its potential for ovarian cancer modelling has still been poorly investigated. In 2011, Xu *et al.*[29] described a Matrigel® based coculture model including ovarian cancer cells and normal fibroblasts. In this work, a home-made bioprinting platform was used to pattern cell encapsulating droplets with a high throughput and a controlled space distribution. However, no further research has been conducted regarding the viability; phenotypic markers of the two cell types; and their potential interactions[29]. The biological relevance of such bioprinted ovarian tumor models thus remains to be demonstrated. To address this question, we used 3D bioprinting to develop a high throughput model of an ovarian tumor. This model comprised cancer cells (SKOV-3 cells) and cancer-associated fibroblasts (MeWo cells) encapsulated in a biocompatible gelatin-alginate hydrogel. In this work, we describe the major steps that were carried out to establish and further characterize this model. These steps included hydrogel optimization; viability and metabolic activity evaluation; histology and immunological studies; and real-time imaging. We believe our 3D bioprinted tumor model to be an interesting preclinical tool to develop therapies against ovarian cancer.

2. Materials and methods

2. 1. Reagents and cell culture

The bioprinter BioX, CELLINK (USA) was used in this study. Sodium alginate, gelatin (type B gelatin, bovine origin), calcium chloride and sodium citrate were purchased from Sigma-Aldrich (St. Louis, MO, USA). SKOV-3 cells (ovarian adenocarcinoma derived cell line) were purchased from Sigma-Aldrich. MeWo cells (ATCC HTB-65TM), granular fibroblasts, derived from human melanoma were purchased from ATCC and used as CAFs.

SKOV-3 cells were cultured in Dulbecco's Modified Eagle Medium (DMEM), supplemented with 10% (v/v) Fetal bovine serum (FBS), 2% L-glutamine, 1% Penicillin-Streptomycin and 0,05% Amphotericin B. MeWo cells were cultured in Minimal Essential Medium (MEM) supplemented with 10% (v/v) FBS, 1% Penicillin-Streptomycin, 0,05% Amphotericin B and 1 mM sodium pyruvate. All cell culture reagents were supplied by Sigma-Aldrich (St. Louis, MO, USA). Both cell lines were cultured in T75 flasks at 37°C, 5% CO₂ and passaged twice a week. Live/Dead Viability/Cytotoxicity Kit for mammalian cells was purchased from Invitrogen, Thermo Fisher Scientific, (USA). Cell proliferation kits including Water-soluble tetrazolium 1 (WST1) kit and Alamar Blue kit were purchased from Roche laboratories (France). Green fluorescent protein (GFP) JetOPTIMUS® transfection kit was kindly provided by Polyplus Transfection company (France). Orange CMRATM Cell tracker, Thermo Fisher Scientific (USA) was kindly provided by Dr. De Isla N. (Ingénierie Moléculaire et Physiopathologie Articulaire (IMoPA), France). Paraformaldehyde 4% (PAF) was supplied by VWR (France). Hematoxylin-Eosin-Safran (HES) kit, HES automated device (Dako CoverStainer®) and immunohistochemistry (IHC) automated device (Dako Omnis IHC®) were purchased from Dako (Santa Clara, USA). The provenance and the concentration of the different antibodies used in this study are mentioned in Section 9, Table 5. CellVue® Claret Far Red Fluorescent Cell Linker Mini Kit for General Membrane Labeling and PKH67 Green Fluorescent Cell Linker Mini Kit for General Cell Membrane Labeling were supplied by Sigma-Aldrich (St. Louis, MO, USA).

2.2. Hydrogel optimization

To develop our bioprinting hydrogel, a combination of two biocompatible polymers was used that are sodium alginate (SA) and gelatin (G). For this optimization phase, DMEM culture medium containing 10% FBS was used as a solvent. To define the optimal hydrogel quantitative

composition, we applied the following strategy. Two sets of hydrogels with different concentrations of gelatin and sodium alginate (Table 1) were assessed for their printability at 37°C. For that, a volume of 10 mL of each solution was prepared as following: the required masses of gelatin and sodium alginate powders were weighted, decontaminated under ultra-violet (UV) rays for 1 hour and incorporated within the solvent in sterile glass vials. Solutions were then kept at 37°C under magnetic steering over night for complete dissolution.

To select the best formulation, solutions were first sorted depending on their ability to form gels at room temperature. All the solutions remaining liquid at room temperature were eliminated as they are not printable at 37°C in a liquid state. Each of the remaining solutions was then submitted to bioprinting trails at 37°C. These trails consisted of printing a square shape of 10x10x1 mm. The printability of each hydrogel was defined through its ability to precisely reproduce the theoretical shape of the square at 37°C (Fig. 1). The hydrogel showing best results in terms of printability was used for the further steps of the study. The experience was performed three times. It has to be mentioned that this square shape is not the final shape selected for our tumor model. However, we still decided to use it for the optimization phase as it is very adequate to visually appreciate the printability of each hydrogel.

Table 1. Different solutions prepared for the hydrogel optimization phase

Set 1				Set 2			
Sodium alginate		Gelatin		Sodium alginate		Gelatin	
w/v %	Required mass for 10 mL solution (g)	w/v %	Required mass for 10 mL solution (g)	w/v %	Required mass for 10 mL solution (g)	w/v %	Required mass for 10 mL solution (g)
1	0.1	1	0.1	2	0.2	1	0.1
1	0.1	3	0.3	2	0.2	3	0.3
1	0.1	5	0.5	2	0.2	5	0.5
1	0.1	7	0.7	2	0.2	7	0.7
1	0.1	9	0.9	2	0.2	9	0.9
1	0.1	11	1.1	2	0.2	11	1.1
1	0.1	13	1.3	2	0.2	13	1.3
1	0.1	15	1.5	2	0.2	15	1.5

2.3. Design of the tumor mass

Our tumor model was designed as a cylinder of 7 mm diameter and 1.5 mm thickness. The online 3D computer assisted design (CAD) platform One Shape was used to create this 3D form which was further included in the data-base of the bioprinter and used to generate the tumor-like constructs.

2.4. Bioink preparation and bioprinting of the tumor models

Herein, the term “bioink” is used to designate the hydrogel supplemented with cells. Table 2 shows the composition of the different bioinks used during this study. Indeed, while the concentration of gelatin and sodium alginate was similar for all bioinks (according to the results of the optimization phase), their composition in terms of cells and solvent was different depending on the considered condition: (i) SKOV-3 cells in mono-culture; (ii) MeWo cells in monoculture or (iii) coculture of SKOV-3 cells and MeWo cells.

Table 2. Composition of the different bioinks used during this study

Condition	Cells	Solvent
SKOV-3 cells in mono-culture	SKOV-3 cells at 0.5×10^6 cell/mL	Complete DMEM (comprising 10% FBS)
MeWo cells in mono-culture	MeWo cells at 0.5×10^6 cell/mL	Complete MEM (comprising 10% FBS)
Coculture of SKOV-3 cells and MeWo cells	SKOV-3 cells + MeWO cells (1:1 ratio) at a final concentration of 10^6 cell/mL (0.5×10^6 cell/mL of SKOV-3 cells + 0.5×10^6 cell/mL of MeWo cells)	Complete DMEM + complete MEM (1:1 ratio)

To make the bioinks, hydrogels with the selected concentration of SA and G were first prepared as described in Section 1. The next day, cells were trypsinized, suspended in adequate culture

media and incorporated within the hydrogels. The obtained bioinks were gently agitated to ensure homogenous cell distribution while minimizing air bubble incorporation.

For bioprinting, bioinks were carefully loaded in 3 ml cartridges, kept at room temperature for 15 to 20 minutes then introduced in the bioprinter printhead. 24 well plates were used as a support for bioprinting and incubation of the tumor models. All further experiments were carried out in 24 well plates unless otherwise stated. Other bioprinting parameters were set as shown in Table 3.

Table 3. Parameters for the bioprinting process

Parameter	Corresponding value
Interne diameter of the printhead needle	23G (0.60 mm)
Printhead temperature	37°C
Printing bed temperature	8°C
Extrusion pressure	10 – 20 kPa
Printhead movement speed	4 – 5 mm/s

After bioprinting, the obtained 3D structures were chemically crosslinked using 500 μ L of a 100 mM calcium chloride (CaCl_2) solution per well for 7 minutes before being washed once with fresh culture medium. Each structure was then supplemented with 1 mL complete culture medium and the plates were incubated at 37°C and 5% CO_2 until further experiments (Fig.2).

2.5. Cell viability

Live/Dead Viability/Cytotoxicity assay was performed on the bioprinted structures according to the manufacturer’s instructions[30]. After eliminating culture medium, 3D bioprinted structures were washed 3 times with DPBS and supplemented with 500 μ l working solution of 4 μ M calcein and 16 μ M ethidium homo-dimer 1 (EthD1). After incubation in the dark for 40 minutes at 37°C, the structures were observed under confocal microscope (Zeiss LSM 710, Heidelberg, Germany) using appropriate filters as shown in Table 4.

Table 4. Parameters of confocal observation during the Live/Dead assay

Reagent	Calcein	Ethidium homo-dimer 1
Excitation / emission wavelengths (nm)	494 / 517	528 / 617
Standard set filters	Green channel:	Red channel:

	(Ex / EM = 488 / 520 nm)	(Ex / EM = 561 / 596 nm)
--	--------------------------	--------------------------

The experiment was performed at days 1, 4 and 7 after bioprinting. For each time-point, negative controls (structures containing dead cells) were prepared by exposing bioprinted structures to 70% Methanol for 30 minutes before treatment with the Live/Dead kit reagents. Three independent experiments were performed. Quantification of Live (green) and Dead (red) cells at day 1 after bioprinting was performed using ImageJ 1.53c free software. Cell viability at day 1 was then expressed as the average percentage of green cells among the whole cell population over the 3 experiments with error corresponding to the standard deviation.

2.6. Metabolic activity and cell proliferation

Cell metabolic activity in tumor models was assessed using two assays, namely WST1 assay and Alamar Blue assay. After discarding the culture medium, bioprinted structures were supplemented with fresh culture medium containing 10% (v/v) of WST1 reagent or Alamar Blue reagent and incubated at 37°C for 5 hours. A volume of 500 μ L of 1.5% (w/v) sodium citrate solution was then added to each structure for 30 minutes to dissolve the matrix and release the dye produced by cells. The resulting solution was transferred to 96 well plate (100 μ L/well, 4 wells for each structure). A microplate reader was used to evaluate absorbance at 450 nm for WST1 assay and fluorescence (Ex/EM = 544/590 nm) for Alamar Blue assay. Negative controls (structures exposed to 70% methanol for 30 minutes) were realized. The experiment was conducted at days 1, 3 and 7 after bioprinting. At least three independent experiments were performed for each assay.

2.7. Cell spatial distribution in the bioprinted structures

To visualize cell spatial distribution in the bioprinted tumor models, SKOV-3 cells and MeWo cells were labeled differently and used to prepare bioprinted structures for confocal microscopy imaging.

SKOV-3 cells were transfected to express GFP using JetOPTIMUS® transfection kit according to the manufacturer's instructions. Briefly, transfection solution was prepared by combining 1 mL buffer, 10 μ g DNA and 10 μ L transfection reagent. After keeping the resulting transfection solution at room temperature for 10 minutes, it was carefully introduced to the culture medium

in a T75 flask of SKOV-3 cells at about 60% confluence. The next day, cells were trypsinized and used for bioprinting.

MeWO cells were labeled using Orange CMRA™ cell tracker according to the user guide instructions[31]. After removing the culture medium, MeWo cells in a T25 flask were exposed to a 20 µM Orange CMRA™ working solution for 30 minutes. The reagent solution was then removed and replaced with complete MEM medium. The next day, cells were trypsinized and used for bioprinting. Confocal images of the bioprinted structures containing labeled cells were taken at day 1 after bioprinting.

2.8. Histology and immunological staining

For histological analysis, bioprinted tumor modes were treated as following: samples were first washed with HBSS for 15 minutes at 37°C then fixed in a 4% PFA solution containing 50 mM CaCl₂ for 1 hour at room temperature. After fixation, structures were again washed twice with HBSS solution for 5 minutes before being dehydrated successively in 70% ethanol, 96% ethanol, 100% ethanol and 100% xylene baths. Samples were then paraffin-embedded, cut into 6 µm thickness sections and HES coloration was performed with DAKO CoverStainer®. Structures were examined at days 1, 3 and 7 after bioprinting. At least three different structures were observed for each time point and three independent experiments were performed.

For immunohistochemistry, bioprinted structures were fixed and paraffin-embedded as described above. After that, samples were cut into 6 µm sections and immunological staining was performed with Dako Omnis® IHC automate.

Following markers were assessed: Ki67, Paired box gene 8 (PAX8), SRY-related HMG-box 10 (SOX10) and vimentin. Antibodies used were as mentioned in Table 5.

Table 5. Antibodies used for IHC

Antibody	Clone and provenance	Dilution
Anti-Ki67	Monoclonal mouse anti-human Ki67 antigen clone Mib1 ; Dako (Santa Clara, CA, USA)	1: 50
Anti-PAX8	Polyclonal rabbit anti-human PAX8; Diagnostics (Blaganc, France)	1: 20

Anti-SOX10	Monoclonal Rabbit anti-human Sox-10 protein clone EP268 (Diagnostic Biosystems, Pleasanton, USA)	1: 200
Anti-vimentin	Monoclonal mouse anti-human vimentin; Clone V9; (Dako, Santa Clara, CA, USA)	1: 200

The expression of Fibroblast Activation Protein (FAP) in the bioprinted structures was assessed by immunofluorescence. For that, structures were fixed and paraffin-embedded as described above. After that, immunofluorescence staining was carried out on 6 μ m thick deparaffinized sections following a manual procedure. Before staining, the sections were subjected to heat-induced epitope retrieval by incubation in tri-sodium citrate buffer solution (pH 6) at 95 °C for 10 min followed by 20 min of cooling. Slices were briefly rinsed with DPBS. The samples on each slide were spotted with Super PAP pen. PBS/BSA 5%, blocking solution was added to each spotted sample for 45 min. In a humidified chamber, primary antibody (Rabbit anti FAP polyclonal antibody, Fisher Scientific (USA)) at 1:100 was diluted in 3% (m/v) BSA and incubated with the samples at room temperature for 1 h. After that, the slices were washed twice with DPBS for 3 min and incubated with secondary antibody, anti-rabbit IgG, Atto 550, Sigma-Aldrich (St. Louis, MO, USA), diluted at 1:100 for 1 h at room temperature. Afterwards, the slices were washed four times with DPBS before covering them with coverslips in the presence of a drop of Vectashield® antifade mounting medium. The slides were then placed at 4°C and observed under an upright epifluorescence microscope (AX-70 Provis, Olympus, Paris, France) the next day.

For immunohistochemistry and immunofluorescence, structures at day 7 after bioprinting were examined. At least three different structures were stained for each marker and three independent experiments were performed.

2.9. Real-time imaging

Real-time imaging experiments were performed on the bioprinted tumor models to observe potential cell migration in the bioprinted structures. For that, the two cell types were labeled differently. SKOV-3 cells were stained with CellVue® Claret Far Red Fluorescent Cell Linker and MeWo cells were stained with the membrane green fluorescent cell marker PKH67 according to the manufacturer's instructions. Briefly, the suspensions of MeWo or SKOV-3 cells were washed once with serum-free medium. The cell pellets were then gently mixed in

the dark with CellVue® or PKH67 working solutions for 10 min (4 μ m reagent + 1 ml diluent for each 10^7 cells). An excess volume of FBS was then added for 2 min to adsorb the non-attached reagent. Cells were then washed twice with complete medium before being incorporated in the hydrogel for bioprinting. Bioprinted structures containing labeled cells were imaged from day 1 to day 7 after bioprinting using the automated cell imaging system ImageXpress®, Pico, Molecular Devices (United Kingdom). Two independent experiments were performed and three different structures were imaged in each experiment.

3. Results and discussion

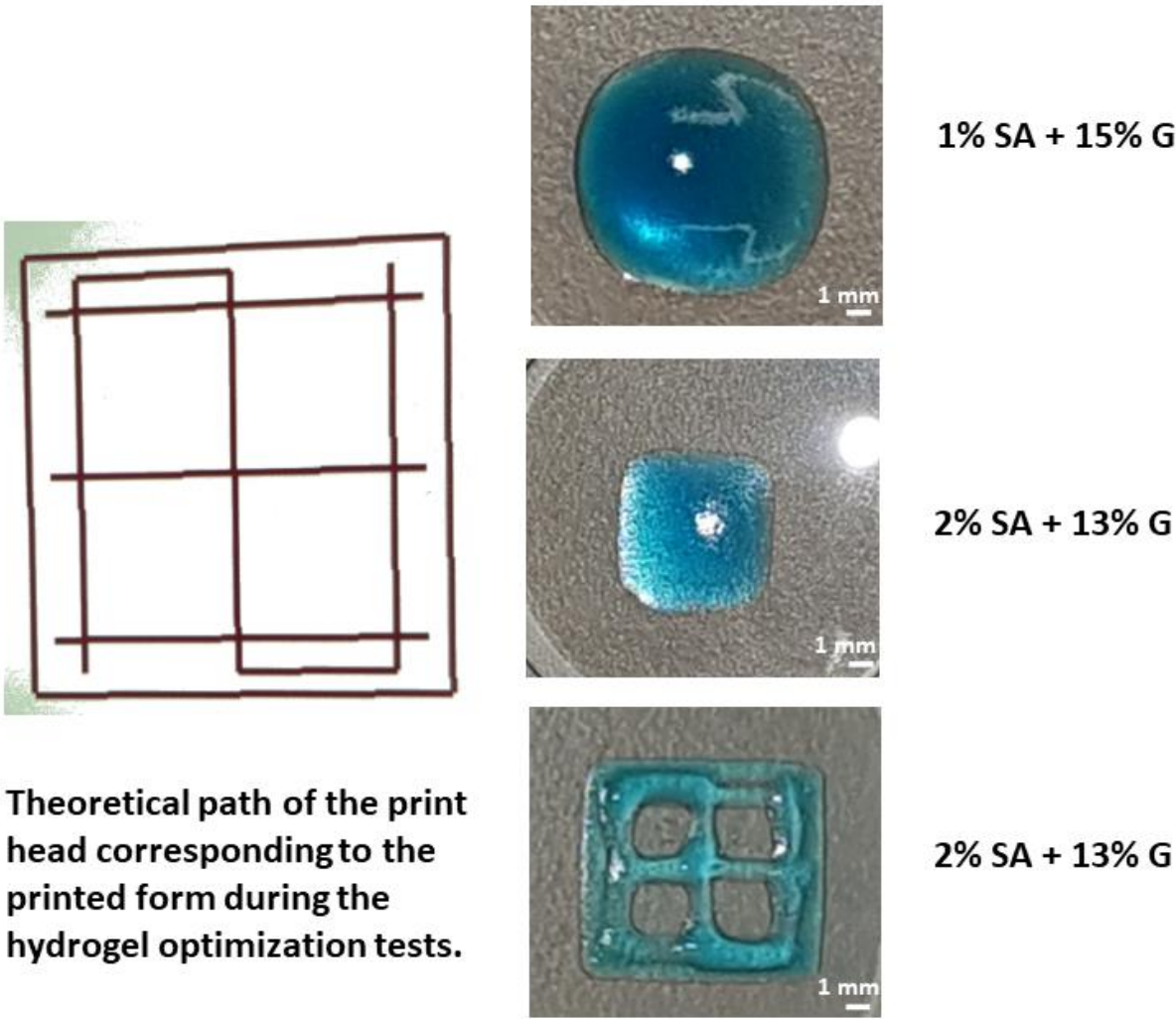
3.1. Hydrogel optimization

While 3D bioprinting is emerging as a revolutionary tool in *in vitro* cancer modelling, it is always important to identify the most appropriate biomaterials for bioink formulation. In this work, a combination of sodium alginate and gelatin was selected to establish the bioprinted ovarian cancer model. Gelatin is a bio-compatible and cost-effective material that favors cell adhesion and proliferation[32]. The inclusion of sodium alginate in the bioink formulation allows easy and rapid chemical crosslinking of the bioprinted structures which is important for long term culture at 37°C. Importantly, it is possible to modulate mechanical properties of gelatin-alginate hydrogels by modifying their respective concentrations. In this work, we used this property to identify the optimal hydrogel quantitative composition that provides best printability at 37°C under minimal extrusion pressure. With this aim, different alginate-gelatin solutions were prepared and assessed for their gel forming behavior at room temperature and printability at 37°C. The solutions containing 1% SA + 1% to 13% gelatin did not form gels at room temperature as well as the solutions containing 2% SA + 1% to 11% gelatin. The remaining solutions including: (1% SA + 15% G), (2% SA + 13% G) and (2% SA + 15% G) did form gels at room temperature and were thus subjected to bioprinting trials. The corresponding results are shown in Figure 1. While the (1% SA + 15% G) and (2% SA + 13% G) solutions did not reproduce the desired square shape, it could easily be printed using the (2% SA + 15% G) solution. This formulation was thus selected for all further experiments. Interestingly, a low extrusion pressure (10 to 20 kPa) was sufficient to achieve a good printing with the (2% SA + 15% G) formulation. This can be highlighted as a significant advantage compared to other recent works where an extrusion pressure of 20 to 100 kPa was reported[33]. Indeed, extrusion pressure is a crucial parameter to be considered while performing bioprinting

experiments. High extrusion pressure was shown to affect cell viability with a viability falling under 80% as the printing pressure goes up to 28 kPa[34].

Figure 1. Bioprinting trials performed during the hydrogel optimization phase. (1% SA + 13%G) and (2% SA + 13% G) solutions were too runny at 37°C and did not show good printability. (2% SA + 15% G) solution could be well printed at 37°C and was thus selected for further experiments. All solutions were colored in blue for better visualization. The experience was performed three times. Representative images are shown. Scale bar = 1 mm.

Bioprinting at 37°C / 10-20 kPa

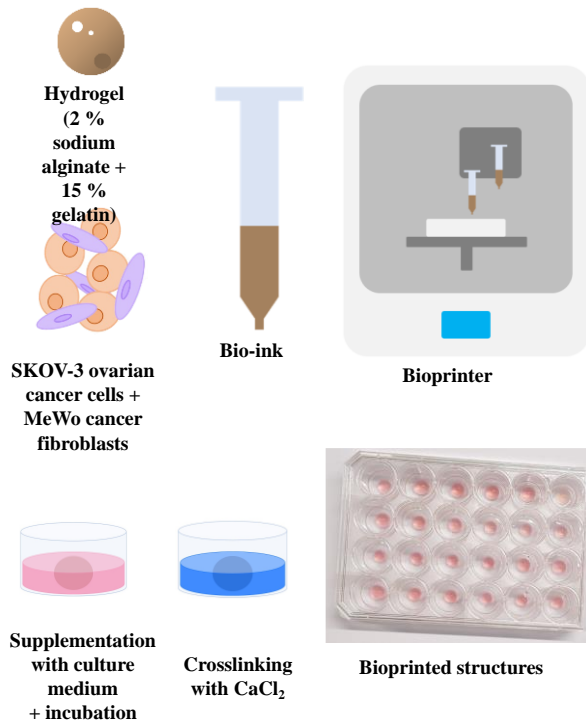


Theoretical path of the print head corresponding to the printed form during the hydrogel optimization tests.

3.2. Bioprinting of tumor models

Figure 2 shows the main steps in the bioprinting process and images of bioprinted tumor models consisting of 7 mm diameter and 1.5 mm thickness cylinders. The shape and dimensions of these bioprinted structures were set to be suitable for further culturing them in a home-made microfluidic device that is not described in this paper. SKOV-3 cells and MeWo cells could be encapsulated in the alginate-gelatin hydrogel at a total density of 1 million cell / mL to form the final bioink. A volume of 3 mL of bioink was sufficient to prepare more than 48 samples with a high reproducibility and within less than 4 hours of manipulation. This is thus a time-effective approach which can be useful for high throughput screening applications. With regard to cost, only the initial investment required for the acquisition of the bioprinter can be substantial. Apart from that, the establishment and culture of the bioprinted structures is extremely cost-effective as it does not require any specific growth factor or culture media. In the long run, this approach can therefore be very advantageous compared to other technologies such as organoids for example.

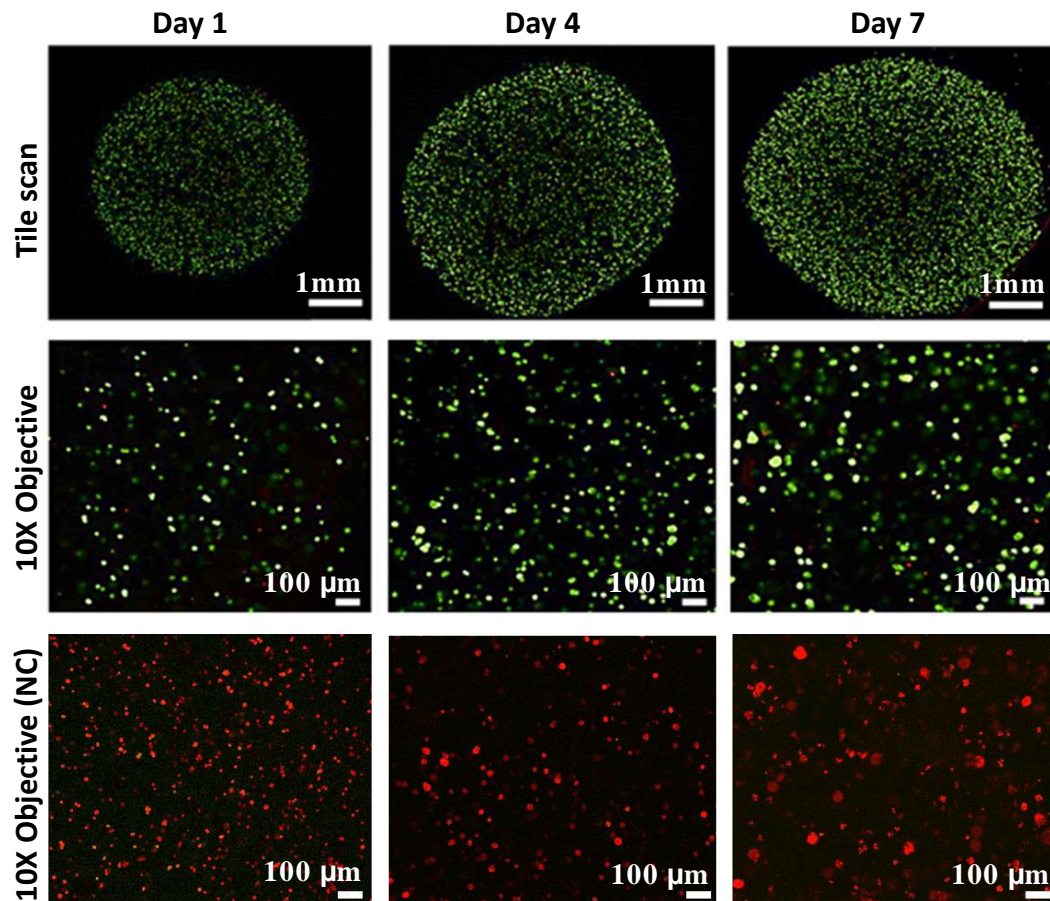
Figure 2. The bioprinting process: Cells are trypsinized and included in the (2% SA + 15% G) hydrogel to form a bioink. Tumor models (cylinders of 7 mm diameter and 1,5 mm thickness) are then printed, crosslinked (CaCl₂ 100 mM; 7 minutes), supplemented with fresh culture medium and incubated at 37°C, 5% CO₂ till further experiments.



3.3. Cell viability and proliferation

Preserving cell viability is a major challenge when performing extrusion-based bioprinting. Cells can be impacted by different parameters including extrusion pressure[34,35], printing speed[34] and crosslinking process[36]. To assess cell viability in the bioprinted tumor models, Live/Dead assay was performed using confocal microscopy. The corresponding results are given in Figure 3. At day 1 after bioprinting, the great majority of the cell population showed green fluorescence (live cells) while red fluorescence (dead cells) was very less. This reflects a high cell viability in the bioprinted tumor-like structures ($91.38\% \pm 10.67\%$) with very few cells being damaged during the printing process. As shown in figure 3, this high viability was maintained at day 4 and even at day 7 after bioprinting. The observation of the tile scan images (Fig. 3, upper panel) also shows that green fluorescence (live cells) is more intense in the structure's periphery when compared to its center. This is attributed to two main reasons. First, cells in the periphery are more exposed to the Live/Dead Kit reagents. Second, cells in the structure's periphery are also more proliferative as they are more exposed to nutrients and oxygen. This supposes the establishment of an oxygen and nutrient gradient over the bioprinted structures which is of major importance in a 3D tumor model. Similar observations with cells intensively invading the peripheral parts of bioprinted structures were made by other groups using other bioinks at a similar cell density[33].

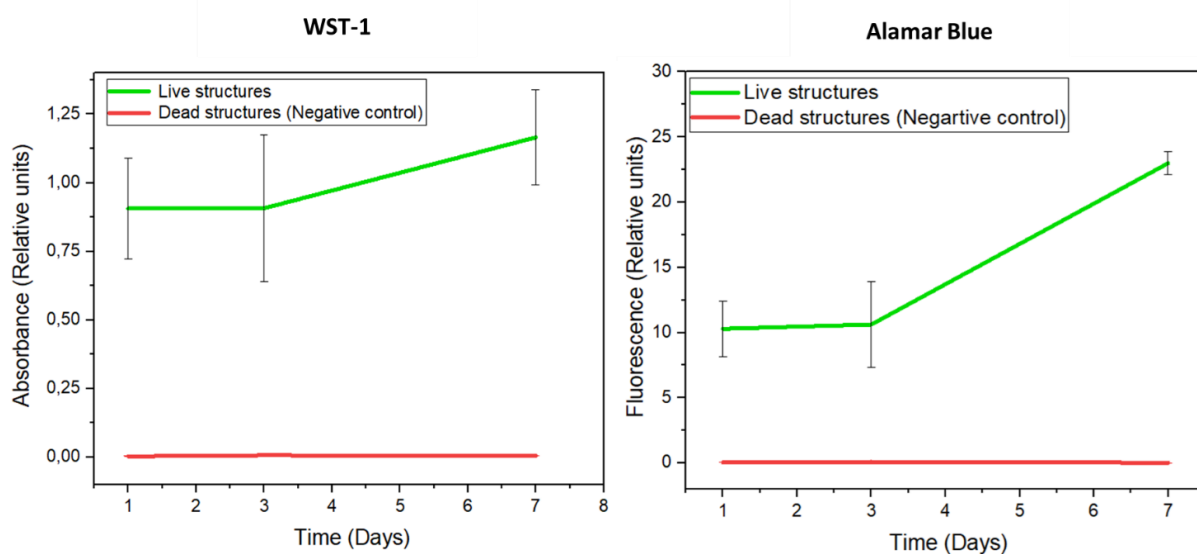
Figure 3. Live/Dead staining followed by confocal microscopy imaging on the bioprinted tumor models. Live cells emit green fluorescence while dead cells emit red fluorescence. Tile scan images were obtained by combining images from multiple acquisition fields (10X objective) to provide an overall view of the bioprinted structure. (NC) designates Negative Control (bioprinted structures exposed to methanol for 30 minutes). Three independent experiments were performed. Representative images are shown.



Cell metabolic activity in the tumor models was evaluated through WST1 assay and Alamar Blue assay (Figure 4). At day 1 after bioprinting, the tumor-like structures (living structures) showed high metabolic activity in comparison with the negative control (structures exposed to methanol for 30 minutes) for both WST1 and Alamar Blue assays. Absorbance measured through WST1 assay was 0.9 ± 0.1 (Absorbance Arbitrary Units (AAU)) for living structures versus 0.003 ± 0.001 AAU for negative control. For Alamar Blue assay, fluorescence measured at day 1 was 10.4 ± 2.1 (Fluorescence Arbitrary Units (FAU)) for living cells versus 0.04 ± 0.001 FAU for negative control. At day 3, WST1 assay and Alamar Blue assay showed

absorbance and fluorescence levels (respectively) comparable to those observed at day 1 pointing out that cells survive the bioprinting process and maintain their metabolic activity. More interestingly, at day 7, the metabolic activity significantly progressed (from 0.90 ± 0.2 AAU at day 4 to 1.16 ± 0.1 AAU at day 7 for WST1 assay and from 10.6 ± 3.2 FAU at day 4 to 22.9 ± 0.8 FAU at day 7 with Alamar Blue assay). This progression in metabolic activity is due to the increased cell number reflecting cell proliferation within the bioprinted structures.

Figure 4. WST1-1 and Alamar Blue assays performed on bioprinted structures containing both SKOV-3 cells and MeWo cells at 0.5×10^6 cell/ mL of bioink for each cell-type (Total cell density = 1×10^6 cell/mL). Negative controls correspond to bioprinted structures treated with 70% methanol for 30 minutes. For WST-1 assay, results are expressed as absorbance values at 450 nm (Absorbance Arbitrary Units (AAU)). For Alamar Blue assay, results are expressed as fluorescence values (ex/em = 544/590 nm) (Fluorescence Arbitrary Units (FAU)). Results are averages from 4 independent experiments for WST-1 and 3 independent experiments for Alamar Blue. Errors bars correspond to standard deviations.

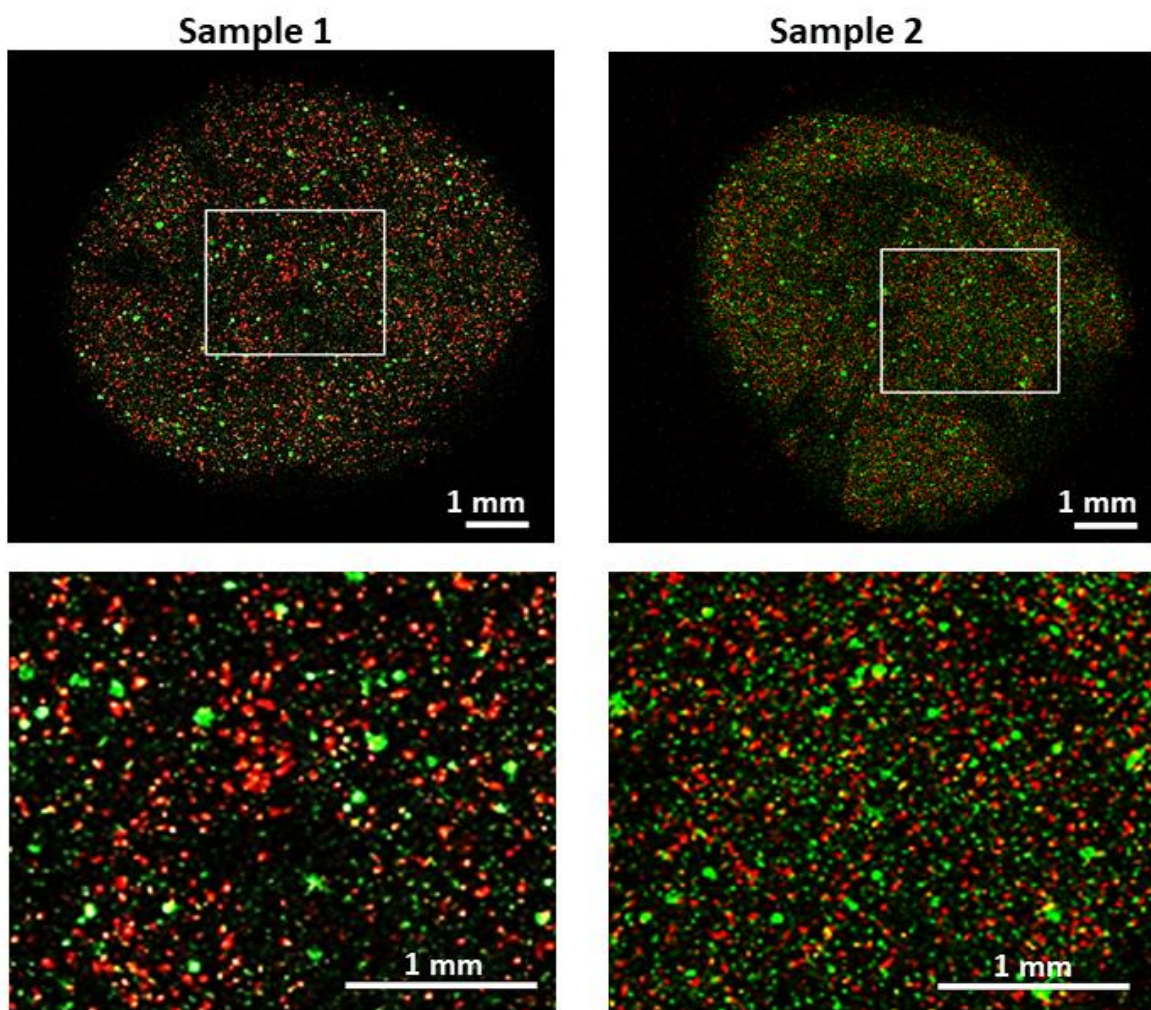


3.4. Cell spatial distribution in the tumor model

Beyond viability and metabolic activity, it was important to assess cell spatial distribution in the bioprinted tumor models. It is currently acknowledged that the *in vivo* tumor microenvironment is composed of different cell types that closely interact with each other[8].

It is therefore crucial for a tumor model to provide a suitable environment to reproduce these intercellular interactions notably by allowing a close cohabitation of cancer cells with other TME elements. The two cell types in our tumor-like model were distinctly labeled before confocal microscopy visualization. As shown in Figure 5, we could observe that the two cell types, cancer cells and cancer-associated fibroblasts, are homogeneously (uniformly) distributed in the bioprinted structures. Such cell proximity is very convenient for the development of *in vivo*-like cell-cell interactions.

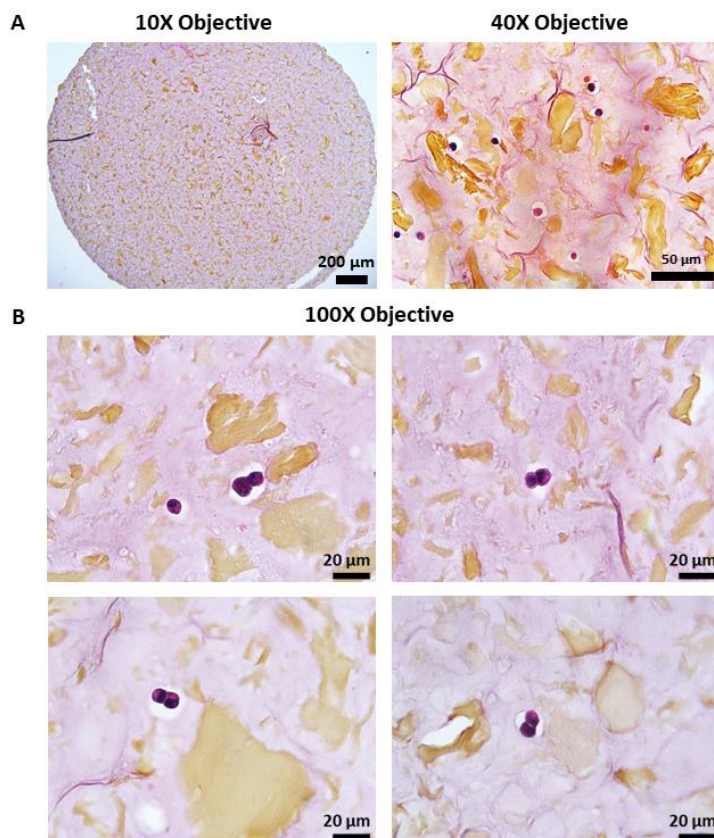
Figure 5. Confocal imaging after distinct labeling of the two cell types at day 1 after bioprinting. SKOV-3 cells were transfected to express GFP (green). MeWo cells were labeled with Orange CMRA™ CellTracker (Orange). The 2 cell types are homogeneously distributed in the matrix. Scal bar = 1mm.



3.5. Histological analysis

Histological studies are key tools for cancer diagnosis and prognosis. Our model was subjected to histological analysis using HES staining to assess cell morphology and distribution in the matrix. Figure 6A shows that cells at day 1 after bioprinting were uniformly distributed in the matrix reflecting the homogenous cell encapsulation in the gelatin-alginate hydrogel. Interestingly, multiple mitotic figures could be visualized already at day 1 after bioprinting as shown in figure 6B. This reflects the maintained cell proliferation in the bioprinted tumor-like structures. Mitotic figures are also a key histological characteristic of *in vivo* high grade epithelial ovarian cancers[37].

Figure 6. Histological analysis (HES staining) of bioprinted structures (coculture condition) at day 1 after bioprinting. A: Cell distribution in the matrix. Cells are individualized and homogeneously distributed within the bioprinted structures. B: Mitotic figures observed at day 1 after bioprinting reflecting maintained cell proliferation. Three independent experiments were performed. Representative images are shown.



Besides maintaining their proliferation, we observed that cells formed increasingly massive clusters within the bioprinted structures (Fig.7 and Fig. S1). Cells thus spontaneously

aggregated to form spheroid-like structures. This generated, over the sections, an alternance of cell-free zones and zones with a high cell density. To quantify the aggregate size evolution over time, we defined, for each aggregate, a small diameter (SDi) and a large diameter (LDi) (as the aggregates are not perfectly circular in shape). We then measured these parameters and assessed their evolution over time. The corresponding results are shown in figure 8 and figure S2. At day 1 after bioprinting, the average aggregate SDi was $20.41 \pm 4.35 \mu\text{m}$ and the average LDi was $27.08 \pm 5.53 \mu\text{m}$. At day 7 after bioprinting, the average SDi increased to reach $31.41 \pm 8.43 \mu\text{m}$. Similarly, the average LDi reached $43.98 \pm 14.63 \mu\text{m}$. The aggregates thus become larger over time as they contain increasing number of cells as shown in figure 7 and figure S1. This tendency of cells to self-organize in spheroid-like clusters within bioprinted structures was reported by several other groups using other cancer cells and other hydrogels[25,33,38]. As it has been suggested by other authors, this may indicate the crucial role the of the three-dimensional environment in driving the organization of cancer cells[33].

Figure 7. Histological analysis (HES) of bioprinted structures (coculture condition, total cell density = 1×10^6 Cell/mL of bioink) showing the evolution of cell distribution over time. Cells form self-assembled aggregates (black arrows). Three independent experiments were performed. Representative images are shown.

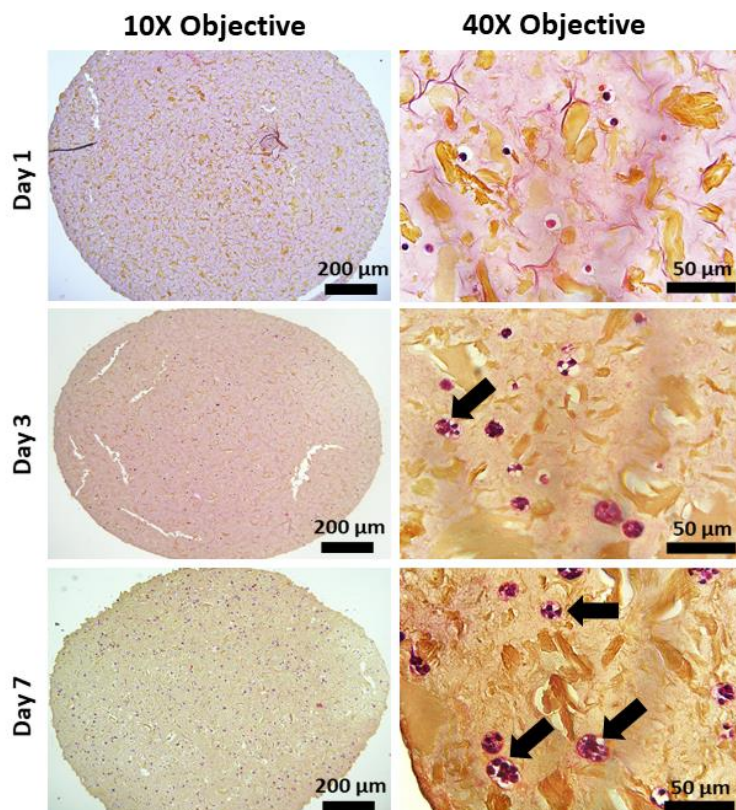
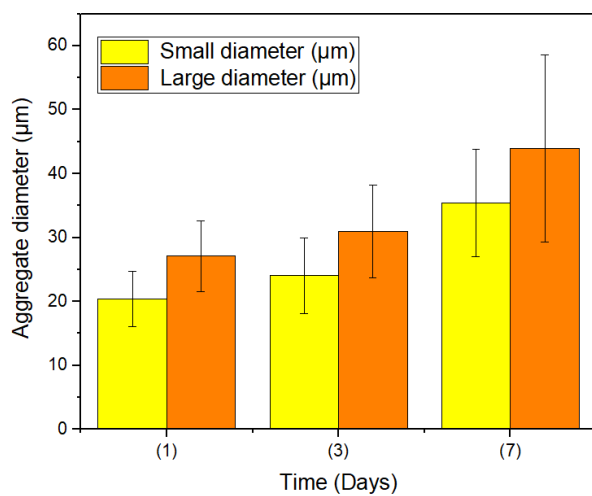


Figure 8. Evolution of aggregate dimensions over time in the bioprinted structures (coculture condition). For each aggregate, a small diameter (SDi) and a large diameter (LDi) were defined. Representative HES images at 40X Objective from three independent experiments were used for performing this analysis. For each time-point, the SDi and the LDi of 50 different aggregates were measured. Average results are represented. Error bars represent Standard deviations (SD).

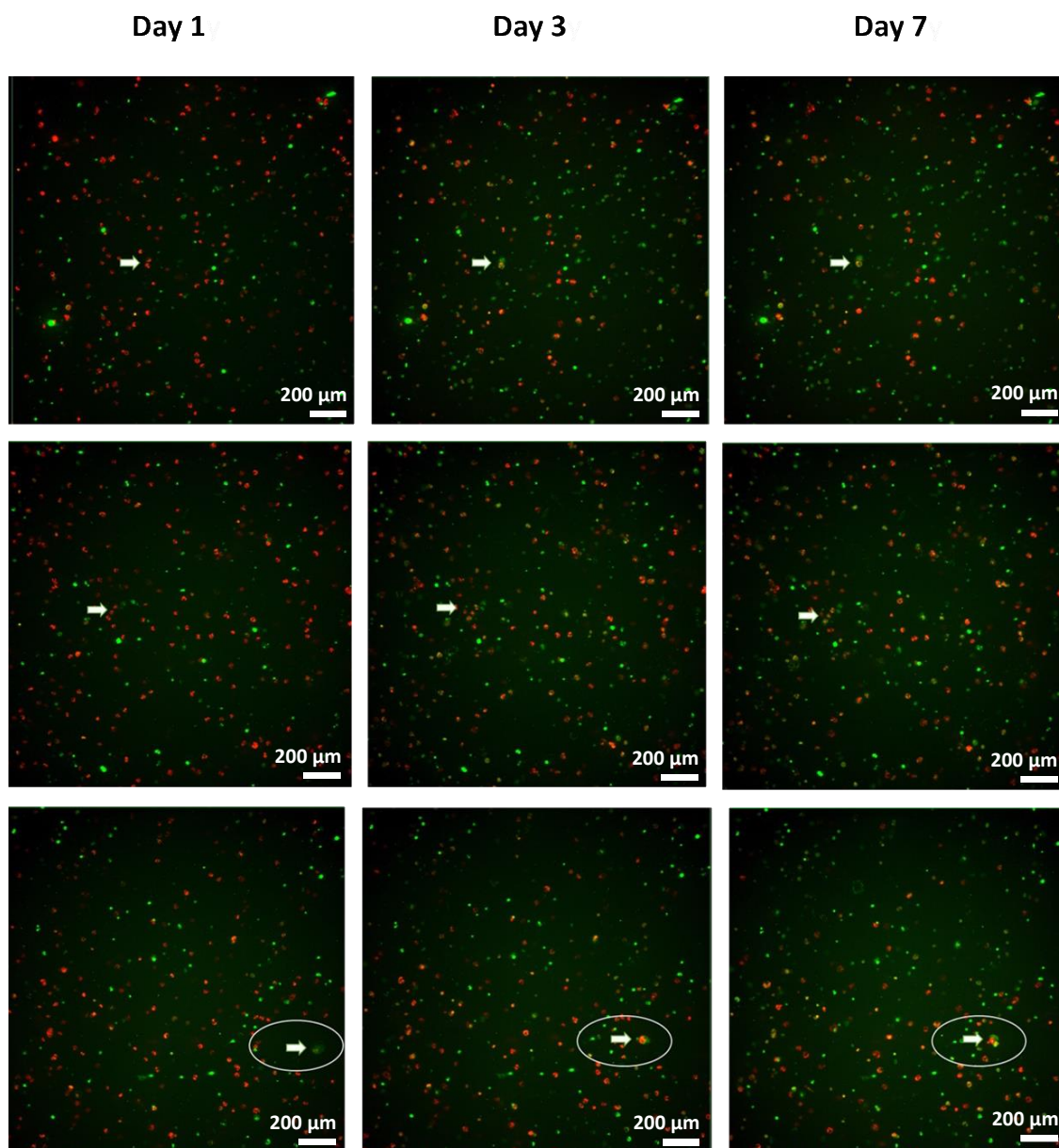


3.6. Real-time imaging:

Histological studies showed that cells in the bioprinted structures were homogeneously dispersed in the matrix at day 1 then self-organized to form increasingly massive clusters allowing an immediate proximity of cells. Thus, we wanted to investigate the mechanism of this self-organization. Namely, we wanted to know whether these clusters arise from successive *in situ* divisions of adjacent cells or from cell migration within the matrix. To answer this question, we performed real-time imaging on the tumor models after differently labeling the two cell types. The corresponding results are shown in Figure 9. Besides migrating within the matrix, MeWo cells were observed to progressively approach SKOV-3 cells. In some fields, MeWo ends up overlapping SKOV-3. Interestingly, similar mechanisms have been reported for *in vivo* tumor development[39]. Rather than remaining as individualized cells, CAFs tend to aggregate and surround carcinoma cells[39]. This tendency of CAFs to circle tumor cells was also described as a potential mechanism of drug resistance[40]. Therefore, in the bioprinted tumor-like structures, cells do not remain static in the hydrogel but reorganize spontaneously,

reproducing pathophysiological phenomena observed *in vivo*, notably CAF recruitment and their organization around cancer cells.

Figure 9. Real-time imaging of bioprinted structures containing SKOV-3 cells (red) and MeWo cells (green). The white arrows show MeWo cells that progressively come into contact with SKOV-3 cells (2 upper panels). MeWo migration in the matrix can also be observed (lower pane). Two independent experiments were performed. Representative images are shown. Scale bar = 200 μm . Full videos are available in the Supplementary information.



3.7. Immunological characterization

For a deeper characterization of our bioprinted tumor-like structures, immunobiological studies were further performed. We first assessed the expression of Ki-67 which is a clinically relevant marker in ovarian cancer diagnosis[37]. Ki-67 identifies cells in the proliferative phase and is associated with poor prognosis in ovarian carcinoma[41]. In our structures, cells were shown to express Ki-67 at day 7 after bioprinting (Fig. 10). This demonstrates the maintained cell proliferation till day 7 after bioprinting. Moreover, this corroborates and explains the results of WST-1 and Alamar Blue metabolic assays. As cells continue to proliferate, this leads to an increased cell number and thus an increased overall metabolic activity within the bioprinted structures. Another immunological marker that is frequently used for ovarian cancer characterization is PAX8[37]. This antigen is usually expressed by all epithelial ovarian cancers[42]. In the monoculture conditions, SKOV-3 cells were found to highly express PAX8 whereas MeWo cells were totally negative for this marker (Fig. 10). In the coculture condition (MeWo + SKOV-3), cell aggregates containing both PAX8 positive cells (SKOV-3 cells) and PAX8 negative cells (MeWo cells) could be identified. This indicates that the observed aggregates are heterotypic (containing the two cell types). To further confirm this initial conclusion, we assessed the expression of a MeWo related marker. We thus selected SOX10, a melanoma specific marker[43] as MeWo cells are malignant melanoma-derived cancer fibroblasts. After showing that this marker was indeed positive for MeWo cells and negative for SKOV-3 cells in monoculture conditions (Fig. 10), we examined the coculture bioprinted structures and we again noticed that SOX10 positive cells and SOX10 negative cells cohabitate in the spheroid-like structures. Our bioprinted model thus offers an ideal three-dimensional environment for close cancer cell – stroma cell cohabitation. We also assessed the expression of vimentin which is a cytoskeleton protein usually expressed by cells of mesenchymal origin including fibroblasts[44]. In our bioprinted models, both MeWo cells and SKOV-3 cells were found to express this protein as SKOV-3 cells were vimentin-positive in the monoculture condition (Fig. 10). This was expected as SKOV-3 cells are known to show an epithelial-mesenchymal phenotype notably characterized by vimentin expression[45] and this specificity was reproduced in our models. As MeWo cells were incorporated in our structures to play the role of cancer-associated fibroblasts (as it has been reported elsewhere[46]), we also performed immunofluorescence imaging to evaluate the expression of a routinely assessed CAF phenotype marker that is FAP[44]. At day 7, MeWo cells did express FAP both in the presence

and in the absence of SKOV-3 cells as is it shown in Figure 11. However, no difference regarding its expression level could be noticed between the two conditions.

Figure 10. Immunohistochemistry (IHC) performed on 3D bioprinted structures to assess the expression of different markers. All sections were performed at day 7 after bioprinting. Both monoculture and coculture conditions were analyzed. 3 independent experiments were performed for each marker. Representative images are shown. Scale bar = 20 μm for all images.

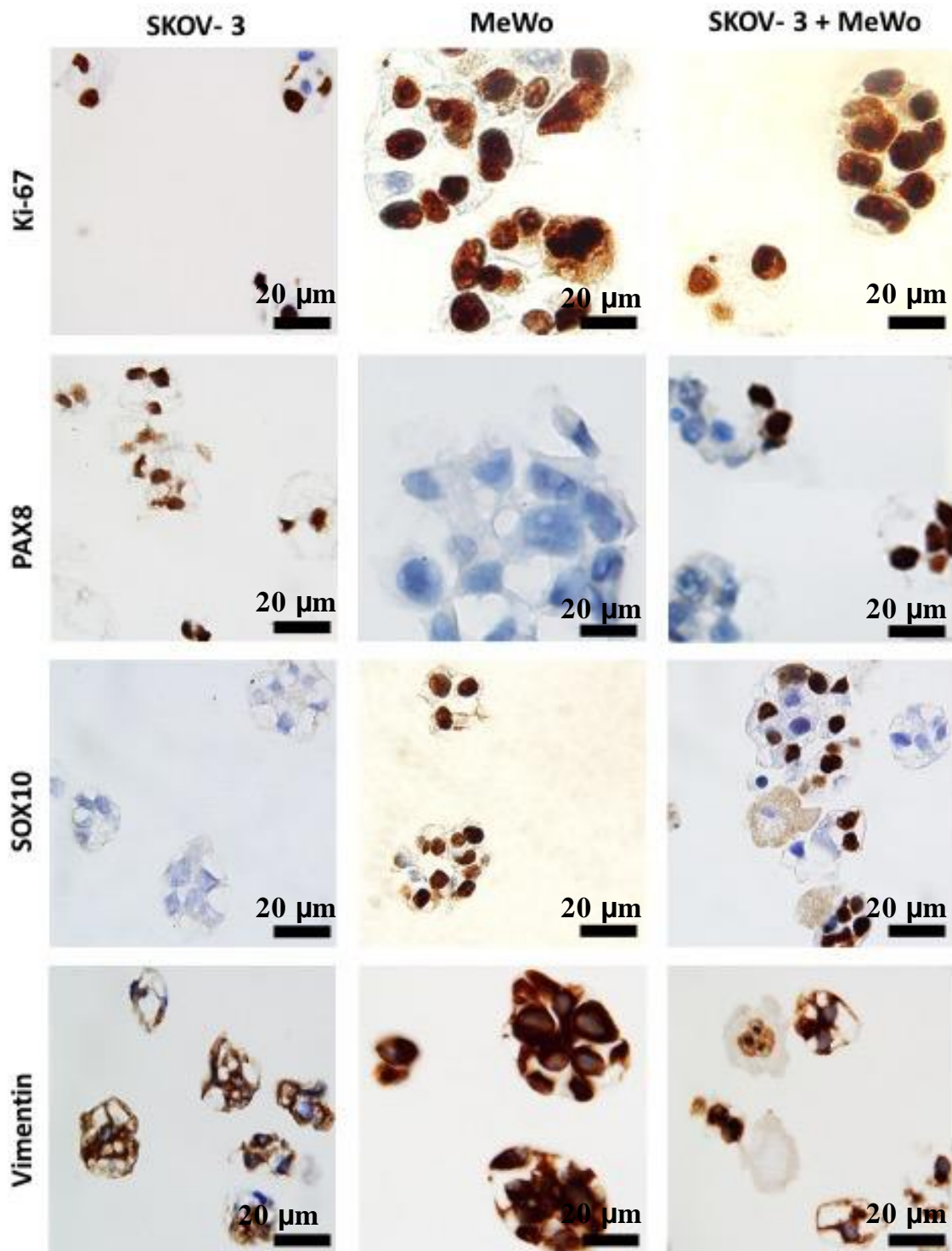
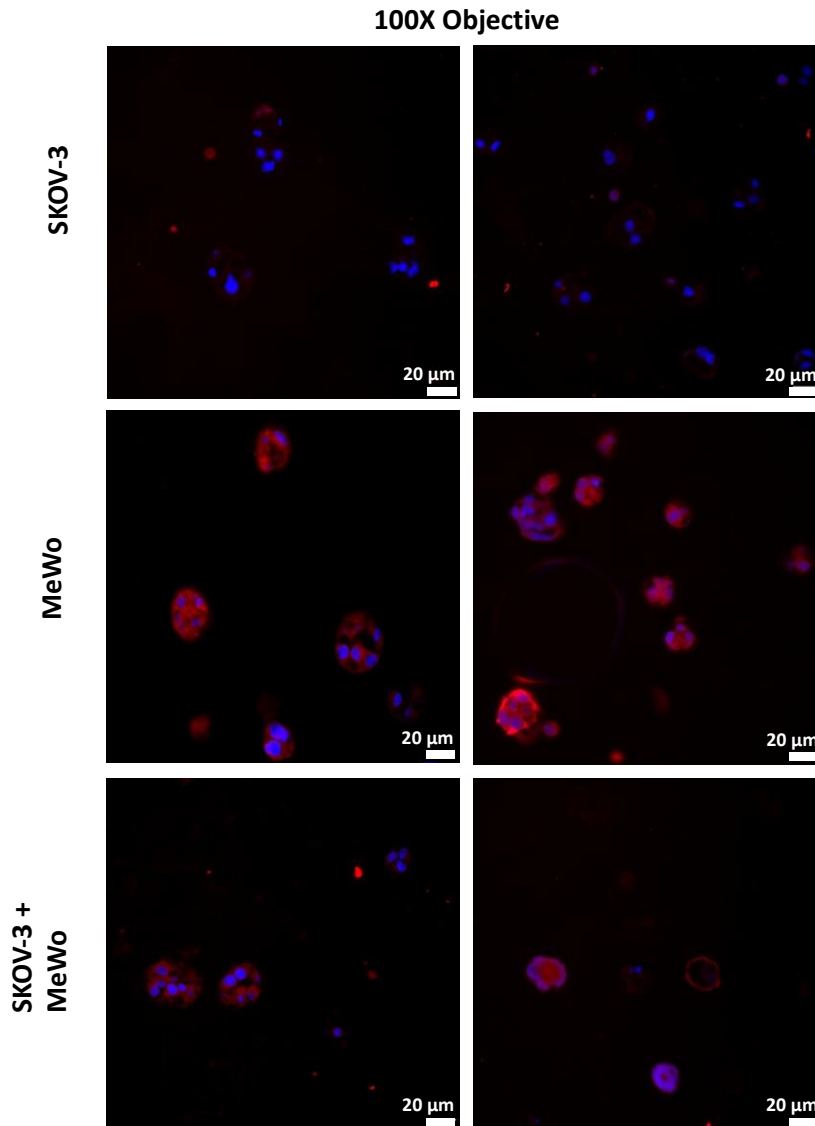


Figure 11. Anti-FAP immunofluorescence staining of sections obtained from bioprinted structures 7 days after bioprinting. Red = FAP expression and Blue = nuclei. Three independent experiments were performed. Representative images are shown. Scale bar = 20 μm for all images.



4. General Discussion

In this study, 3D bioprinting was used to set-up a three-dimensional ovarian tumor model combining cancer cells and cancer-associated fibroblasts. Taken together, the aforementioned results show that the (2% SA + 15%G) hydrogel ensured good printability at a physiological temperature (37°C) and minimal extrusion pressure of 10 to 20 kPa. Combining this hydrogel with these printing parameters allowed to produce bioprinted tumor-like structures with high cell viability and maintained proliferation ability. Cell viability was found to be higher than 90% at day 1 after bioprinting. Also, cell metabolic activity increased from day 3 to day 7 reflecting cell proliferation within the bioprinted structures. This was confirmed through histological analysis that showed cells to self-organize into spheroid-like aggregates whose size increased from day 1 to day 7 after bioprinting. This cell proliferation and aggregation may also

explain the increasing green fluorescence intensity observed over time in the tile scan images obtained after Live/Dead staining (Fig.3; Upper panel). Through real-time imaging, we could observe that the developed cell clusters resulted not only from successive cell division but also from cell migration within the matrix (Fig. 9 and Videos in the supplementary information). Furthermore, cells were shown to maintain the expression of their specific markers and to closely cohabitate in the newly formed heterotypic aggregates. However, one limitation of the model described here-in may be the lack of endothelial cells and immune cells that are important actors in the TME. We made this choice in this study for two main reasons. (i): Very few studies using 3D bioprinting to model ovarian tumors have been described so far. This led us to adopt a step-by-step approach in investigating this research area. And (ii): Although vasculature is undoubtedly a crucial component of ovarian TME[47], some processes are not totally dependent on it. For example, ovarian cancer metastasis occurs primarily via non-hematogenous dissemination[48]. Another limit of this study is that our bioprinted structures could not be kept in culture for more than 7 days. After that, they became too loose and no more usable for carrying out experiments. A such short time window makes these bioprinting models inadequate to study long-term processes taking place in the TME. Nevertheless, we strongly believe that further investigations on hydrogel formulation will allow to build more complex and more time-durable models.

Conclusions:

Developing more predictive preclinical cancer models is becoming an emergency to bridge the gap between conventional 2D models and the *in vivo* complexity. 3D bioprinting is emerging as a revolutionary approach to build more *in vivo*-like tumor tissues. In this work, extrusion-based 3D bioprinting was used to build an ovarian tumor model. For that, we used a home-made, cost-effective bioink whose composition could be optimized to insure good printability at 37°C and a minimal extrusion pressure. To the best of our knowledge, this is the first bioprinting-based ovarian tumor model where several biological characterizations were performed including viability and proliferation assays; histology and immunological staining; and real-time imaging. Through these studies, we first could evidence the high cell viability in our tumor model thus highlighting the biocompatibility of our home-made bioink. Besides remaining viable and proliferative, cells in the bioprinted structures self-organized into heterotypic aggregates while maintaining the expression of their key phenotype markers such as PAX8 for SKOV-3 cells and FAP for MeWo cells. This bioprinting approach can thus be a

powerful tool to establish patient-specific tumor models for capturing the inter-patient tumor heterogeneity. Importantly, we could also demonstrate that 3D bioprinted tumor models can easily be subjected to different assay routinely used in cancer research including viability assays; metabolic activity measurement; histology and immunological staining. This makes them adequate tools for anticancer drug evaluation. Therefore, we believe 3D bioprinting to be a versatile technology that can create a paradigm-shift in tissue engineering and cancer modeling.

Funding:

This research was funded by: The University Institute of France; the Algerian Government and Interdisciplinarite project Capu (Université Lorraine)

Data Availability Statement:

The data generated during this study are available from the corresponding author upon reasonable request.

Acknowledgments:

We sincerely thank Dr. Natalia De Isla and Meriem Hadid (IMOPA, University of Lorraine) for providing reagents for confocal imaging

Conflicts of interest:

The authors declare no conflict of interest.

References

1. Sung, H., Ferlay, J., Siegel, R.L., Laversanne, M., Soerjomataram, I., Jemal, A., et Bray, F. (2021) Global Cancer Statistics 2020: GLOBOCAN Estimates of Incidence and Mortality Worldwide for 36 Cancers in 185 Countries. *CA Cancer J. Clin.*, **71** (3), 209-249.
2. Menon, U., Gentry-Maharaj, A., Burnell, M., Singh, N., Ryan, A., Karpinskyj, C., Carlino, G., Taylor, J., Massingham, S.K., Raikou, M., Kalsi, J.K., Woolas, R., Manchanda, R., Arora, R., Casey, L., Dawnay, A., Dobbs, S., Leeson, S., Mould, T., Seif, M.W., Sharma, A., Williamson, K., Liu, Y., Fallowfield, L., McGuire, A.J., Campbell, S., Skates, S.J., Jacobs, I.J., et Parmar, M. (2021) Ovarian cancer population screening and mortality after long-term follow-up in the UK Collaborative Trial of Ovarian Cancer Screening (UKCTOCS): a randomised controlled trial. *The Lancet*, **397** (10290), 2182-2193.

3. Lisio, M.-A., Fu, L., Goyeneche, A., Gao, Z., et Telleria, C. (2019) High-Grade Serous Ovarian Cancer: Basic Sciences, Clinical and Therapeutic Standpoints. *Int J Mol Sci*, **20** (4), 952.
4. Thibault, B., Castells, M., Delord, J.-P., et Couderc, B. (2014) Ovarian cancer microenvironment: implications for cancer dissemination and chemoresistance acquisition. *Cancer Metastasis Rev*, **33** (1), 17-39.
5. Kapałczyńska, M., Kolenda, T., Przybyła, W., Zajączkowska, M., Teresiak, A., Filas, V., Ibbs, M., Bliźniak, R., Łuczewski, Ł., et Lamperska, K. (2018) 2D and 3D cell cultures – a comparison of different types of cancer cell cultures. *Arch Med Sci*, **14** (4), 910-919.
6. Xu, H., Lyu, X., Yi, M., Zhao, W., Song, Y., et Wu, K. (2018) Organoid technology and applications in cancer research. *J Hematol Oncol*, **11**, 116.
7. Ghoneum, A., Afify, H., Salih, Z., Kelly, M., et Said, N. (2018) Role of tumor microenvironment in ovarian cancer pathobiology. *Oncotarget*, **9** (32), 22832-22849.
8. Anderson, N.M., et Simon, M.C. (2020) The tumor microenvironment. *Curr Biol*, **30** (16), R921-R925.
9. Zhang, Y., Tang, H., Cai, J., Zhang, T., Guo, J., Feng, D., et Wang, Z. (2011) Ovarian cancer-associated fibroblasts contribute to epithelial ovarian carcinoma metastasis by promoting angiogenesis, lymphangiogenesis and tumor cell invasion. *Cancer Lett.*, **303** (1), 47-55.
10. Zhang, F., Cui, J., Gao, H., Yu, H., Gao, F., Chen, J., et Chen, L. (2020) Cancer-associated fibroblasts induce epithelial-mesenchymal transition and cisplatin resistance in ovarian cancer via CXCL12/CXCR4 axis. *Future Oncol.*, **16** (32), 2619-2633.
11. Langhans, S.A. (2018) Three-Dimensional in Vitro Cell Culture Models in Drug Discovery and Drug Repositioning. *Front. Pharmacol.*, **9**, 6.
12. SANTINI, M.T., RAINALDI, G., et INDOVINA, P.L. (1999) Multicellular tumour spheroids in radiation biology. *Int. J. Radiat. Biol.*, **75** (7), 787-799.
13. Cui, X., Hartanto, Y., et Zhang, H. (2017) Advances in multicellular spheroids formation. *J. R. Soc. Interface*, **14** (127), 20160877.
14. Tuveson, D., et Clevers, H. (2019) Cancer modeling meets human organoid technology. *Science*, **364** (6444), 952-955.
15. Driehuis, E., Kretschmar, K., et Clevers, H. (2020) Establishment of patient-derived cancer organoids for drug-screening applications. *Nat. Protoc.*, **15** (10), 3380-3409.
16. Nanki, Y., Chiyoda, T., Hirasawa, A., Ookubo, A., Itoh, M., Ueno, M., Akahane, T., Kameyama, K., Yamagami, W., Kataoka, F., et Aoki, D. (2020) Patient-derived ovarian cancer organoids capture the genomic profiles of primary tumours applicable for drug sensitivity and resistance testing. *Sci Rep*, **10** (1), 12581.

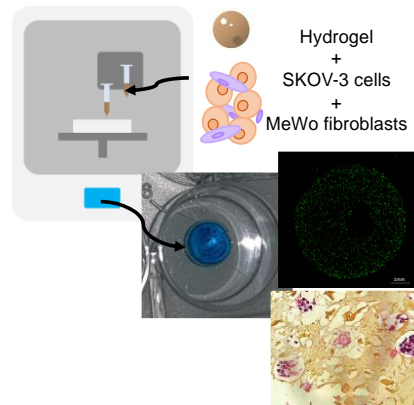
17. Lee, S.H., Hu, W., Matulay, J.T., Silva, M.V., Owczarek, T.B., Kim, K., Chua, C.W., Barlow, L.J., Kandoth, C., Williams, A.B., Bergren, S.K., Pietzak, E.J., Anderson, C.B., Benson, M.C., Coleman, J.A., Taylor, B.S., Abate-Shen, C., McKiernan, J.M., Al-Ahmadie, H., Solit, D.B., et Shen, M.M. (2018) Tumor Evolution and Drug Response in Patient-Derived Organoid Models of Bladder Cancer. *Cell*, **173** (2), 515-528.e17.
18. Aboulkheyr Es, H., Montazeri, L., Aref, A.R., Vosough, M., et Baharvand, H. (2018) Personalized Cancer Medicine: An Organoid Approach. *Trends Biotechnol*, **36** (4), 358-371.
19. Hermida, M.A., Kumar, J.D., Schwarz, D., Lavery, K.G., Di Bartolo, A., Ardron, M., Bogomolniji, M., Clavreul, A., Brennan, P.M., Wiegand, U.K., Melchels, F.P.W., Shu, W., et Leslie, N.R. (2020) Three dimensional in vitro models of cancer: Bioprinting multilineage glioblastoma models. *Adv. Biol. Regul*, **75**, 100658.
20. Augustine, R., Kalva, S.N., Ahmad, R., Zahid, A.A., Hasan, S., Nayeem, A., McClements, L., et Hasan, A. (2021) 3D Bioprinted cancer models: Revolutionizing personalized cancer therapy. *Transl. Oncol*, **14** (4), 101015.
21. Tan, B., Gan, S., Wang, X., Liu, W., et Li, X. (2021) Applications of 3D bioprinting in tissue engineering: advantages, deficiencies, improvements, and future perspectives. *J. Mater. Chem. B*, **9** (27), 5385-5413.
22. Kang, H.-W., Lee, S.J., Ko, I.K., Kengla, C., Yoo, J.J., et Atala, A. (2016) A 3D bioprinting system to produce human-scale tissue constructs with structural integrity. *Nat Biotechnol*, **34** (3), 312-319.
23. Tian, T., Ho, Y., Chen, C., Sun, H., Hui, J., Yang, P., Ge, Y., Liu, T., Yang, J., et Mao, H. (2022) A 3D bio-printed spheroids based perfusion in vitro liver on chip for drug toxicity assays. *Chin. Chem. Lett.*, **33** (6), 3167-3171.
24. Albanna, M., Binder, K.W., Murphy, S.V., Kim, J., Qasem, S.A., Zhao, W., Tan, J., El-Amin, I.B., Dice, D.D., Marco, J., Green, J., Xu, T., Skardal, A., Holmes, J.H., Jackson, J.D., Atala, A., et Yoo, J.J. (2019) In Situ Bioprinting of Autologous Skin Cells Accelerates Wound Healing of Extensive Excisional Full-Thickness Wounds. *Sci Rep*, **9** (1), 1856.
25. Wang, X., Zhang, X., Dai, X., Wang, X., Li, X., Diao, J., et Xu, T. (2018) Tumor-like lung cancer model based on 3D bioprinting. *3 Biotech*, **8** (12), 501.
26. Wang, Y., Shi, W., Kuss, M., Mirza, S., Qi, D., Krasnoslobodtsev, A., Zeng, J., Band, H., Band, V., et Duan, B. (2018) 3D Bioprinting of Breast Cancer Models for Drug Resistance Study. *ACS Biomater. Sci. Eng.*, **4** (12), 4401-4411.
27. Dai, X., Ma, C., Lan, Q., et Xu, T. (2016) 3D bioprinted glioma stem cells for brain tumor model and applications of drug susceptibility. *Biofabrication*, **8** (4), 045005.
28. Wang, X., Li, X., Ding, J., Long, X., Zhang, H., Zhang, X., Jiang, X., et Xu, T. (2021) 3D bioprinted glioma microenvironment for glioma vascularization. *J Biomed. Mater. Res. A.*, **109** (6), 915-925.

29. Xu, F., Celli, J., Rizvi, I., Moon, S., Hasan, T., et Demirci, U. (2011) A three-dimensional in vitro ovarian cancer coculture model using a high-throughput cell patterning platform. *Biotechnol J*, **6** (2), 204-212.
30. LIVE/DEAD™ Viability/Cytotoxicity Kit, for mammalian cells.
31. CellTracker™ Orange CMRA Dye.
32. Giuseppe, M.D., Law, N., Webb, B., A. Macrae, R., Liew, L.J., Sercombe, T.B., Dilley, R.J., et Doyle, B.J. (2018) Mechanical behaviour of alginate-gelatin hydrogels for 3D bioprinting. *J Mech Behav Biomed Mater*, **79**, 150-157.
33. Bojin, F., Robu, A., Bejenariu, M.I., Ordodi, V., Olteanu, E., Cean, A., Popescu, R., Neagu, M., Gavriluc, O., Neagu, A., Arjoca, S., et Păunescu, V. (2021) 3D Bioprinting of Model Tissues That Mimic the Tumor Microenvironment. *Micromachines*, **12** (5), 535.
34. Fakhruddin, K., Hamzah, M., et Razak, S.I.A. (2018) Effects of extrusion pressure and printing speed of 3D bioprinted construct on the fibroblast cells viability. *IOP Conf. Ser.: Mater. Sci. Eng.*, **440**, 012042.
35. Nair, K., Gandhi, M., Khalil, S., Yan, K.C., Marcolongo, M., Barbee, K., et Sun, W. (2009) Characterization of cell viability during bioprinting processes. *Biotechnol. J.*, **4** (8), 1168-1177.
36. GhavamiNejad, A., Ashammakhi, N., Wu, X.Y., et Khademhosseini, A. (2020) Crosslinking Strategies for 3D Bioprinting of Polymeric Hydrogels. *Small*, **16** (35), 2002931.
37. Kim, J., Park, E.Y., Kim, O., Schilder, J.M., Coffey, D.M., Cho, C.-H., et Bast, R.C. (2018) Cell Origins of High-Grade Serous Ovarian Cancer. *Cancers (Basel)*, **10** (11), 433.
38. Zhao, Y., Yao, R., Ouyang, L., Ding, H., Zhang, T., Zhang, K., Cheng, S., et Sun, W. (2014) Three-dimensional printing of Hela cells for cervical tumor model. *Biofabrication*, **6** (3), 035001.
39. Karagiannis, G.S., Poutahidis, T., Erdman, S.E., Kirsch, R., Riddell, R.H., et Diamandis, E.P. (2012) Cancer-Associated Fibroblasts Drive the Progression of Metastasis through both Paracrine and Mechanical Pressure on Cancer Tissue. *Mol Cancer Res*, **10** (11), 1403-1418.
40. Neumann, C.C.M., von Hörschelmann, E., Reutzel-Selke, A., Seidel, E., Sauer, I.M., Pratschke, J., Bahra, M., et Schmuck, R.B. (2018) Tumor–stromal cross-talk modulating the therapeutic response in pancreatic cancer. *HBPD INT*, **17** (5), 461-472.
41. Fulawka, L., et Halon, A. (2016) Proliferation Index Evaluation in Breast Cancer Using ImageJ and ImmunoRatio Applications. *Anticancer Res.*, **36** (8), 3965-3972.
42. Liliac, L., Carcangiu, M.L., et Canevari, S. (2013) The value of PAX8 and WT1 molecules in ovarian cancer diagnosis. *Rom J Morphol Embryol.*, **54** (1), 17-27.

43. Willis, B.C., Johnson, G., Wang, J., et Cohen, C. (2015) SOX10: A Useful Marker for Identifying Metastatic Melanoma in Sentinel Lymph Nodes. *ppl. Immunohistochem. Mol. Morphol. APPL IMMUNOHISTO M M*, **23** (2), 109-112.
44. Nurmik, M., Ullmann, P., Rodriguez, F., Haan, S., et Letellier, E. (2020) In search of definitions: Cancer-associated fibroblasts and their markers. *Int J Cancer*, **146** (4), 895-905.
45. Yi, B.-R., Kim, T.-H., Kim, Y.-S., et Choi, K.-C. (2015) Alteration of epithelial-mesenchymal transition markers in human normal ovaries and neoplastic ovarian cancers. *Int. J. Oncol.*, **46** (1), 272-280.
46. Yakavets, I., Jenard, S., Francois, A., Maklygina, Y., Loschenov, V., Lassalle, H.-P., Dolivet, G., et Bezdetnaya, L. (2019) Stroma-Rich Co-Culture Multicellular Tumor Spheroids as a Tool for Photoactive Drugs Screening. *JCM*, **8** (10), 1686.
47. Bamberger, E.S., et Perrett, C.W. (2002) Angiogenesis in epithelial ovarian cancer. *Mol Pathol*, **55** (6), 348-359.
48. Pradeep, S., Kim, S.W., Wu, S.Y., Nishimura, M., Chaluvally-Raghavan, P., Miyake, T., Pecot, C.V., Kim, S.-J., Choi, H.J., Bischoff, F.Z., Mayer, J.A., Huang, L., Nick, A.M., Hall, C.S., Rodriguez-Aguayo, C., Zand, B., Dalton, H.J., Arumugam, T., Jeong, L.H., Han, H.D., Cho, M.S., Rupaimoole, R., Mangala, L.S., Sehgal, V., Oh, S.C., Liu, J., Lee, J.-S., Coleman, R.L., Ram, P., Lopez-Berestein, G., Fidler, I.J., et Sood, A.K. (2014) Hematogenous metastasis of ovarian cancer: Rethinking mode of spread. *Cancer Cell*, **26** (1), 77-91.

Table of Content (ToC)

3D Bioprinted ovarian tumor model



3D bioprinting was used to establish an ovarian tumor model containing cancer cells and cancer-associated fibroblast. The two cell types maintained their viability and proliferation in the bioprinted structures. Cells self-organized into heterotypic aggregates while maintaining the expression of their specific markers. Usual viability and imaging techniques could be applied on our model making it an interesting tool for drug screening.